



Stability of fluorite-type $\text{La}_2\text{Ce}_2\text{O}_7$ under extreme conditions



F.X. Zhang^{a, b, *}, C.L. Tracy^c, M. Lang^d, R.C. Ewing^e

^a Department of Earth and Environmental Sciences, The University of Michigan, Ann Arbor, MI 48109, USA

^b State Key Laboratory of Metastable Materials Science & Technology, Yanshan University, Qinhuangdao, Hebei 066004, China

^c Department of Materials Science and Engineering, The University of Michigan, Ann Arbor, MI 48109, USA

^d Department of Nuclear Engineering, University of Tennessee, Knoxville, TN 37966, USA

^e Department of Geological Sciences, Stanford University, Stanford, CA 94305, USA

ARTICLE INFO

Article history:

Received 31 July 2015

Received in revised form

2 February 2016

Accepted 2 March 2016

Available online 3 March 2016

Keywords:

$\text{La}_2\text{Ce}_2\text{O}_7$

Phase transition

Extreme condition

ABSTRACT

The structural stability of fluorite-type $\text{La}_2\text{Ce}_2\text{O}_7$ was studied at pressure up to ~40 GPa and under hydrothermal conditions of ~1 GPa and up to 350 °C, respectively, using synchrotron X-ray diffraction (XRD) and Raman scattering measurements. XRD measurements indicated that the fluorite-type $\text{La}_2\text{Ce}_2\text{O}_7$ is not stable at pressures greater than 22.6 GPa and gradually transformed to a high-pressure phase. The high-pressure phase is not stable and changed back to the fluorite-type structure when pressure is released. The $\text{La}_2\text{Ce}_2\text{O}_7$ fluorite is also not stable under hydrothermal conditions and began to react with water at 200–250 °C. Both Raman and XRD results suggest that lanthanum hydroxide $\text{La}(\text{OH})_3$ and La^{3+} -doped CeO_2 fluorite are the dominant products after hydrothermal treatment.

© 2016 Elsevier B.V. All rights reserved.

1. Introduction

Most oxides with $\text{A}_2\text{B}_2\text{O}_7$ composition crystallize as a stable, isometric pyrochlore structure, where the BO_6 octahedra form a corner-sharing framework, and the larger A cations and another O reside in the voids of the framework. There are only 4 independent atoms in the unit cell, A and B cations on the 16d and 16c Wyckoff sites, respectively, and two anions on the 48f and 8b sites. In some cases, the two cations A and B share to occupy both cationic sites (16c and 16d), resulting in cation anti-site defects. There are several empty sites, such as 8a and 32e, in pyrochlore structure that can be partially occupied by anions in some cases. The coexistence of cation antisite defects and anion Frenkel defects in the structure is an intrinsic feature of the pyrochlore compounds [1–5]. The pyrochlore structure has a very flexible stoichiometry. Due to the cation and anion defects in the lattice, pyrochlores possess interesting physical, chemical, electrical and magnetic properties, and thus have many potential applications [6–10]. The ion conductivity of pyrochlore oxides has been studied for several decades [11] and some anion-deficient pyrochlores with high ionic conductivity are promising candidates to replace the traditional YZO electrode

materials of solid oxide fuel cells [12–14]. Because of the flexible chemical composition and tunable band gap, some pyrochlore oxides can be used as catalysts [15]. As stable high temperature ceramics, pyrochlore oxides, such as $\text{La}_2\text{Zr}_2\text{O}_7$ and $\text{Gd}_2\text{Zr}_2\text{O}_7$, are used as coatings for high-temperature thermal barriers [16]. Rare earth zirconates with pyrochlore or derivative fluorite structure have also been proposed as the new generation host materials of radioactive waste because of their extreme radiation resistance [17–23].

Understanding defect formation mechanisms in complex oxides is a very important step for the rational development of advanced materials. Previous investigations have suggested that the structure of $\text{A}_2\text{B}_2\text{O}_7$ oxides strongly depends on the ratio of cation radius: r_A/r_B . The pyrochlore structure is only stable to systems with $1.46 < r_A/r_B < 1.78$ [1,9] at ambient conditions. If the A and B cations are of the right relative sizes ($r_A/r_B < 1.46$), a disordered, fluorite-structure will form. A layered perovskite structure is stable when there is a large size difference between the cations, such as in the case for $\text{La}_2\text{Ti}_2\text{O}_7$ [24]. Most rare-earth titanate and stannate with the $\text{A}_2\text{B}_2\text{O}_7$ stoichiometry form an ordered pyrochlore structure, in which RE^{3+} and $\text{Ti}^{4+}/\text{Sn}^{4+}$ occupy the A- and B-site, respectively. However, cation disorder is intrinsic to most rare earth zirconates. The pyrochlore structure is only stable to $\text{RE}_2\text{Zr}_2\text{O}_7$ with rare earth elements lighter than gadolinium, while a disordered, fluorite structure is stable for all of the heavier rare earth elements. In most cases, the cation and anion disorder exist simultaneously in most rare earth zirconates. The oxidation state of cerium is variable and it

* Corresponding author. Department of Earth and Environmental Sciences, The University of Michigan, Ann Arbor, MI 48109, USA.

E-mail address: zhangfx@umich.edu (F.X. Zhang).

can be in either tri- or tetra-valence, and Ce^{4+} is more stable in oxidation environment, which has a compatible size (0.87 Å, 6-fold coordination) with that of Zr^{4+} (0.72 Å). Like Ti^{4+} and Zr^{4+} , Ce^{4+} can replace Zr^{4+} in $\text{RE}_2\text{Zr}_2\text{O}_7$ compounds and form pyrochlore or defect-fluorite structures. The eight-coordinated La^{3+} and six-coordinated Ce^{4+} in $\text{La}_2\text{Ce}_2\text{O}_7$ has a size ratio of $r_A/r_B = 1.33$, which suggests that $\text{La}_2\text{Ce}_2\text{O}_7$ may form as a defect-fluorite structure. Previous density functional theory calculations [25] indicated that pyrochlore structure is energetically favored over the fluorite structure for $\text{La}_2\text{Ce}_2\text{O}_7$, while both XRD and neutron diffraction results are inconsistent with the calculations [26,27]. In fact, the phase stability of pyrochlore- and fluorite-type structures in La–Ce–O system may depend on the ratio of $\text{La}^{3+}/\text{Ce}^{4+}$. Recent neutron diffraction and X-ray absorption experiments [15] have revealed that stoichiometric $\text{La}_2\text{Ce}_2\text{O}_7$ forms a fully-disordered fluorite-type structure AO_{2-x} ($x = 0.25$). La^{3+} and Ce^{4+} share the 4a site in the structure, and the oxygen vacancies are randomly distributed over the anion sublattice.

Rare earth titanates and zirconates with pyrochlore or fluorite structures have been studied under different extreme conditions before, such as high pressure [28–30] and energetic ion irradiation [31–33]. $\text{La}_2\text{Ce}_2\text{O}_7$ has shown promising performance both as an oxide ion conductor [34] and as an electrode component in proton conducting fuel cells [35,36], and also as hydrogen permeation membrane [37]. The operation in different environmental conditions will greatly affect its properties and performance. Study of structural sustainability of materials at various extreme environments is very important for their implication. However, the structural stability at hydrothermal conditions and the reaction of pyrochlore or fluorite oxides with water have not been reported before. In this paper, the structural stability of $\text{La}_2\text{Ce}_2\text{O}_7$ at room temperature/high pressure and hydrothermal conditions (~1 GPa, 350 °C) are investigated.

2. Experimental methods

The starting material of $\text{La}_2\text{Ce}_2\text{O}_7$ was prepared by traditional solid-state reaction method from the corresponding binary oxides La_2O_3 (Alfa Aesar, 99.9% purity) and CeO_2 (Alfa Aesar, 99.5% purity). La_2O_3 powder was preheated at 800 °C for 5–12 h before weighing in order to remove the absorbed moisture from air. The powder of La_2O_3 and CeO_2 in 1:2 M ratio was well mixed with a mortar and pestle in acetone medium and then pressed into a pellet with a hydrostatic press. The pellet was first baked at 1300 °C for 24 h in air, reground into powder and pressed into a pellet again. The pellet was then heated at 1400 °C for another 24 h. The single phase structure of the synthetic sample was confirmed from the X-ray diffraction profile measured with a Rigaku Miniflex X-ray diffractometer (Cu K α). For the room temperature high-pressure experiments, the sample was pressurized in a symmetric diamond anvil cell with methanol/ethanol (4:1 volume ratio) or He as the pressure medium. Ruby or Au powder was used as a pressure marker for the experiments. The *in situ* XRD measurement was conducted at beam-line 16BMD, HPCAT, Advanced Photon Source with X-ray wave length of 0.4957 Å. The Debye rings were collected with a MAR345 image detector and then integrated into one-dimensional XRD profiles with program Fit2d [38]. The pressure in the chamber with He pressure medium was also calibrated by the change of the unit cell parameter of Au from its equation of state [39]. For hydrothermal experiments, a small amount of $\text{La}_2\text{Ce}_2\text{O}_7$ sample was loaded together with deionized water into a hydrothermal diamond anvil cell (HDAC-V) together with ruby chips for pressure calibration. The mixture of sample and water were first pressurized to 1.0 GPa and then heated up to 350 °C with 50 °C temperature steps. The temperature was held for 10 min at each step before the

XRD measurement. The instrumental parameters, including sample-detector distance were calibrated with CeO_2 powder as an external standard. A similar hydrothermal experiment was done for the Raman measurements, but with higher pressure and temperature conditions (~10 GPa, 485 °C). Rietveld refinement analysis of the XRD profiles was completed with the program Fullprof in Winplotr [40]. The structure for the samples quenched from ambient temperature/high-pressure with the M/E medium and from hydrothermal experiments were also checked with synchrotron XRD measurements.

3. Results and discussion

The disordered, fluorite-structure of the synthetic $\text{La}_2\text{Ce}_2\text{O}_7$ sample was confirmed by XRD analysis. There were no diffraction peaks of the pyrochlore superlattice. Fig. 1 shows the XRD pattern refined with the defect fluorite structure as the model structure [15]. Though we have refined all the possible parameters, including scale factor, temperature factors and orientation coefficients, there are still observable difference in the intensity of diffractions (111), (222) and (311), which may be due to the large grain size and stress in the lattice. Of course, the intensity difference has little effect on the lattice constant during refinement. The refined unit cell constant, $a = 5.5645$ (2) Å, is very close to the unit cell parameter (5.5657 Å) measured by neutron powder diffraction [15]. In order to study the phase stability at high pressure, $\text{La}_2\text{Ce}_2\text{O}_7$ samples was pressurized to 39.6 GPa with helium as pressure medium and 42.8 GPa with methanol/ethanol pressure medium. Fig. 2 shows the selected XRD profiles of $\text{La}_2\text{Ce}_2\text{O}_7$ with He as the pressure medium. Weak diffraction maxima from the Au powder—the pressure marker, were observed and marked with * in the XRD pattern at 3 GPa. Starting at 22.6 GPa, a broad weak diffraction peak appeared at 2θ angle of ~9.5°. This is the strongest diffraction maximum from the high-pressure phase. Like other pyrochlore or fluorite oxides, the pressure-induced phase transition in $\text{La}_2\text{Ce}_2\text{O}_7$ is sluggish and only the diffraction maxima from the high-pressure phase and Au are observed in the XRD patterns at 35.4 and 39.6 GPa. The high-pressure phase of $\text{La}_2\text{Ce}_2\text{O}_7$ shows very broad diffraction peak(s) in the 2θ range of 9–11° and several weaker broad peaks at higher 2θ range. The XRD profile of the high-pressure phase is very similar to that of nanocrystalline or amorphous phases. Pressure-induced amorphization has been previously observed in $\text{Gd}_2\text{Ti}_2\text{O}_7$ pyrochlore during release of pressure [29], but the high-pressure phase

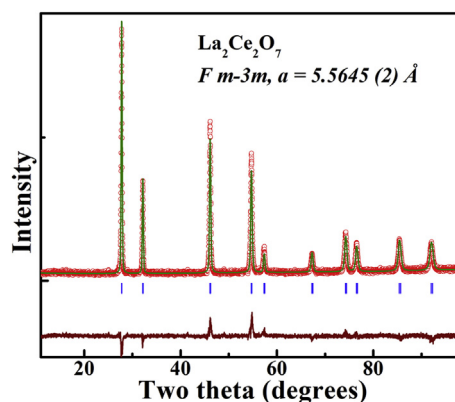


Fig. 1. The XRD pattern (lab X-ray with Cu K α radiation) of $\text{La}_2\text{Ce}_2\text{O}_7$ refined with a fluorite structure model (Space group: $Fm\bar{3}m$, La/Ce: 4a (0, 0, 0); O: 8c ($\frac{1}{4}$, $\frac{1}{4}$, $\frac{1}{4}$)). The refinement yields lattice constant $a = 5.5645$ (2) Å with $R_p = 8.46\%$, $R_{wp} = 10.4\%$, $R_B = 9.12\%$, $R_f = 4.96\%$, $\chi^2 = 1.54$. The imperfect fit for the intensities of diffractions (111), (222) and (311) is mainly due to the large grain size and stress in the powder sample.

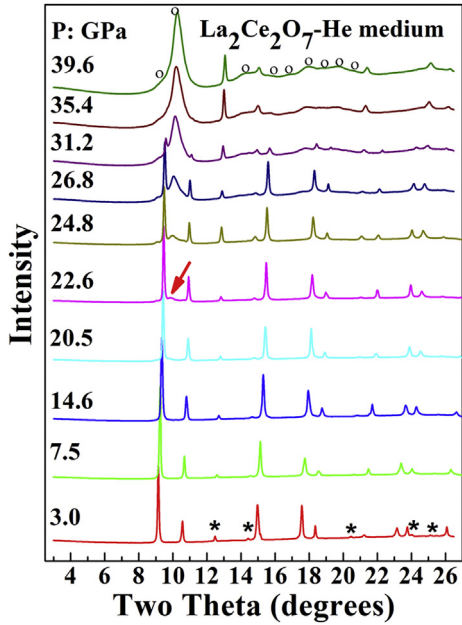


Fig. 2. XRD profiles of $\text{La}_2\text{Ce}_2\text{O}_7$ at high pressure conditions with He pressure medium. The peaks marked with star are from gold which is a pressure marker. The peaks marked with “o” represent possible diffractions from the high-pressure phase and the arrow in the pattern at 22.6 GPa is the main peak of the high-pressure phase. (For interpretation of the references to colour in this figure legend, the reader is referred to the web version of this article.)

of $\text{La}_2\text{Ce}_2\text{O}_7$ is not amorphous. The asymmetric broad peak in the XRD pattern at high pressures is, in fact, composed of several overlapped diffraction peaks. The reversible changes in the XRD patterns during release of pressure in the following experiment also suggest that the high-pressure phase is not amorphous. The high-pressure phase of pyrochlores was previously assumed to be similar to the cotunnite-type structure [41]. However, it is difficult to solve the structural details for the high-pressure phase because of the severe overlap of the diffraction peaks. The high-pressure phase has nanometer scale grain size, which was observed before in quenched pyrochlores [33] by TEM analysis. Previous research revealed that pressure-induced phase transition in $\text{RE}_2\text{Zr}_2\text{O}_7$ pyrochlore or distorted-fluorite structure is reversible [30]. Quick unloading of pressurized sample with He pressure medium may easily break the diamond anvils because of the strain generated by the penetration of He across the diamond surface layer at high pressure conditions. In order to check the structural change of $\text{La}_2\text{Ce}_2\text{O}_7$ during release of pressure, we reloaded $\text{La}_2\text{Ce}_2\text{O}_7$ sample with methanol/ethanol pressure medium and collected XRD patterns during pressure loading and unloading process. The structural change with M/E pressure medium is very similar to the case with helium medium, but has a slightly lower critical transition pressure (21 GPa). Fig. 3 shows the XRD profiles of $\text{La}_2\text{Ce}_2\text{O}_7$ with M/E pressure medium during pressure release. The high-pressure phase is still the dominant at a pressure of 3.3 GPa, however, the quenched sample has mainly the fluorite structure, although a weak broad diffraction maximum from the high-pressure phase is still present in our experiment time scale.

In order to obtain the bulk modulus of the fluorite $\text{La}_2\text{Ce}_2\text{O}_7$, the XRD profiles were refined with Rietveld method using a fluorite-structure model [15], in which La^{3+} and Ce^{4+} share the 4a site. The lattice constant and unit cell volume at different pressures are listed in Table 1. Fig. 4 shows the P–V curve of $\text{La}_2\text{Ce}_2\text{O}_7$ up to 31 GPa. Fitting with 3rd order Birch–Murnaghan equation of state yields a bulk modulus of 144 GPa, and the pressure derivative

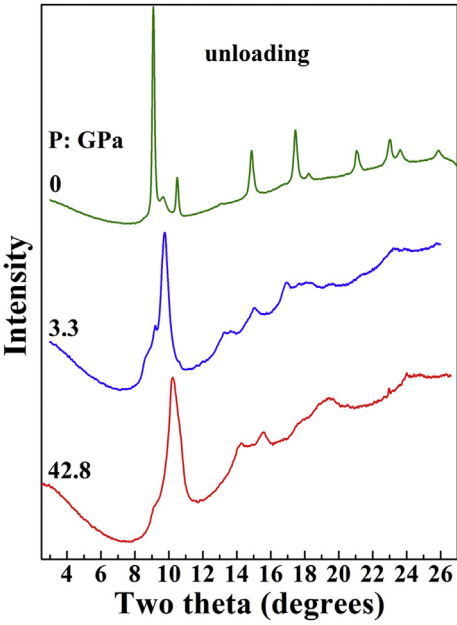


Fig. 3. The XRD patterns of $\text{La}_2\text{Ce}_2\text{O}_7$ during release of pressure (methanol/ethanol pressure medium). The pressure-induced phase transition in $\text{La}_2\text{Ce}_2\text{O}_7$ is reversible and the quenched sample gradually changed back to fluorite-type structure.

Table 1
The lattice parameter and unit cell volume of the cubic fluorite $\text{La}_2\text{Ce}_2\text{O}_7$ at various pressures derived from Rietveld refinement.

P (GPa)	a (Å)	V (Å ³)	P (GPa)	a (Å)	V (Å ³)
1 0	5.5642 (2)	172.30 (1)	8 17.0	5.3886 (1)	156.47 (1)
2 3.0	5.5288 (1)	169.00 (1)	9 20.5	5.3619 (2)	154.15 (1)
3 5.2	5.5040 (2)	166.74 (1)	10 22.6	5.3444 (2)	152.65 (1)
4 7.5	5.4693 (2)	163.60 (1)	11 24.8	5.3273 (2)	151.19 (1)
5 10.2	5.4323 (2)	160.31 (1)	12 26.8	5.3088 (2)	149.62 (1)
6 12.2	5.4318 (2)	160.26 (1)	13 29.1	5.2874 (3)	147.82 (2)
7 14.6	5.4081 (2)	158.18 (1)	14 31.2	5.2705 (6)	146.40 (3)

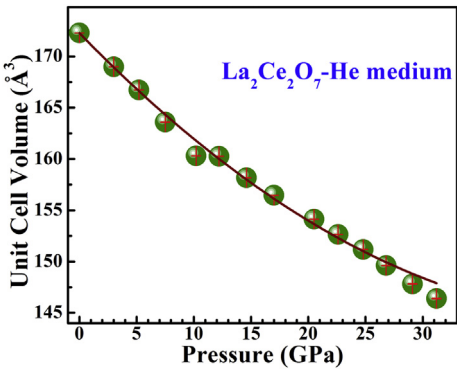


Fig. 4. The experimental P–V curve of fluorite-type $\text{La}_2\text{Ce}_2\text{O}_7$ till to ~31 GPa and the solid line is the result fitting with Birch–Murnaghan equation of state.

$B_0' = 3.77$. The bulk modulus is obviously less than other pyrochlore oxides, such as $\text{Gd}_2\text{Zr}_2\text{O}_7$ (186 GPa [42]) and fluorite oxides, such as $\text{Er}_2\text{Zr}_2\text{O}_7$ (279 GPa [30]). This may be due to the large radius of La^{3+} and Ce^{4+} , which expands the cubic structure with more “free volume”.

Fig. 5 shows the Raman spectrum of $\text{La}_2\text{Ce}_2\text{O}_7$ under hydro-thermal conditions. The intensity of Raman active modes for

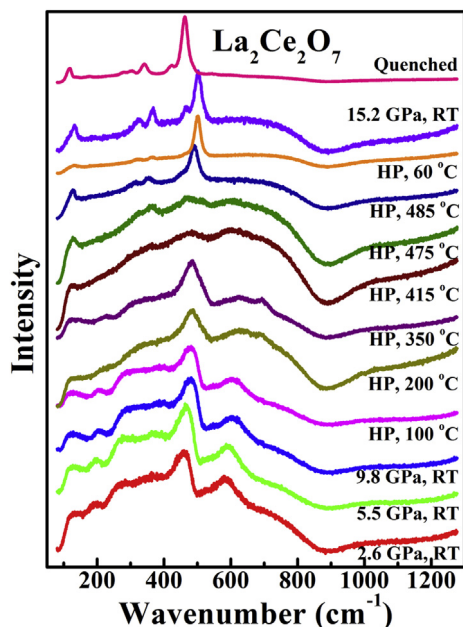


Fig. 5. Raman scattering spectrum of $\text{La}_2\text{Ce}_2\text{O}_7$ at hydrothermal environments. The maximum pressure and temperature is 9.8 GPa and 485 °C, respectively. The final product shows a totally different Raman spectrum compared to the starting material.

$\text{La}_2\text{Ce}_2\text{O}_7$ is generally low at ambient conditions, and it shows one most intense mode at $\sim 450\text{ cm}^{-1}$, one broad mode at $\sim 590\text{ cm}^{-1}$ and 3–4 weak modes in lower frequencies. The ideal fluorite structure has only one allowed Raman active mode (F_{2g}), which corresponds to the vibration of oxygen atoms around the cation. The Raman active mode for undoped CeO_2 with fluorite structure is centered at 465 cm^{-1} [43]. McBride et al. [43] have systematically investigated RE^{3+} doping effect on the Raman modes of fluorite CeO_2 . With the increase of La^{3+} or other rare earth elements in CeO_2 , the F_{2g} mode shifts to lower frequency and becomes asymmetric. The shift of F_{2g} mode is mainly due to the expansion of the structure when La^{3+} is incorporated into the fluorite-structure. The broad band at high frequency arises from the oxygen vacancy as indicated by theoretical calculations and are also observed in La^{3+} -doped ceria [43]. From a structural perspective, the fluorite-type $\text{La}_2\text{Ce}_2\text{O}_7$ can be regarded as a heavily doped (50%) CeO_2 with oxygen vacancies. The shift of the F_{2g} mode was 6 cm^{-1} in 20% atom La-doped CeO_2 [43] and is 15 cm^{-1} in $\text{La}_2\text{Ce}_2\text{O}_7$. The weak bands at low frequency observed in $\text{La}_2\text{Ce}_2\text{O}_7$ sample may also be partially due to the second-order and forbidden acoustic modes caused by defects in the structure [44].

The mixture of $\text{La}_2\text{Ce}_2\text{O}_7$ and water was first pressurized to $\sim 9.8\text{ GPa}$ in a diamond anvil cell and then electrically heated to a temperature of 485 °C. $\text{La}_2\text{Ce}_2\text{O}_7$ has no sharp Raman active modes because of the intrinsic structural defects. There is no obvious change for the spectrum during pressurization, which suggests that the fluorite-type structure is stable before heating. After heating to 200 °C, the spectrum has changed in the region of $\sim 300\text{ cm}^{-1}$, and the broad band at $\sim 590\text{ cm}^{-1}$ became weak and a very broad band between 600 and 800 cm^{-1} appeared. We did not detect good intensity for the band at 450 cm^{-1} during further heating, but another mode with a close frequency grew gradually. At 485 °C, all the bands became sharp and clear, which suggests that there is obvious structural changes. Then the sample was quenched to room temperature within the diamond anvil cell by switching off the power. At room temperature, the measured pressure in the chamber increased to 15.2 GPa. The increase is relatively high as

compared with other minerals during hydrothermal process [45]. This is probably related to the incorporation of molecular water into the fluorite structure, which increases the unit cell volume [46]. At least 5 Raman active modes were observed, which are completely different from those observed in the untreated sample. These Raman modes persist at ambient conditions. The distinct Raman spectrum of the quenched sample indicates that $\text{La}_2\text{Ce}_2\text{O}_7$ fluorite is not stable under high-pressure and high-temperature conditions and reacted with water.

In order to trace the reaction process in detail, an *in situ* synchrotron XRD measurement was performed for the sample in hydrothermal diamond anvil cell. This time, $\text{La}_2\text{Ce}_2\text{O}_7$ was pressurized with water to a pressure of $\sim 1\text{ GPa}$ and then heated to 350 °C. Fig. 6 shows the XRD patterns of $\text{La}_2\text{Ce}_2\text{O}_7$ during heating experiments. The fluorite-structure dominated till 200 °C. The XRD pattern at 250 °C is obviously different from the pattern for the starting materials. A strong diffraction peak grows at the low 2θ angle of $\sim 5^\circ$. At 350 °C, all the diffraction maxima become sharp and clear. The one or two halos in the two theta range of $5\text{--}10^\circ$ are contributed by the diffraction of glass windows in the hydrothermal diamond anvil cell, which were used to prevent oxidation of diamond at high temperatures. A similar background is shown in Fig. 7. Identification of the XRD profiles at high temperature suggests that the sample is hexagonal, with a minor amount of the fluorite-type phase. Comparing the observed lattice parameters with those of all possible products in La–Ce–O system, the hexagonal phase was confirmed to be La/Ce hydroxide and the fluorite is similar with the starting material but with much smaller unit cell constant. The XRD patterns at 250 °C and 300 °C show complex weak diffraction peaks at 2θ angle larger than 12° , which suggests that there may be some intermediate structures formed during heating. Fig. 7 shows the XRD profiles at high temperature (350 °C) and ambient conditions (the sample quenched from Raman measurements). The XRD patterns of both samples can be refined with lanthanide hydroxide and a fluorite-type structure (CeO_2) and the fitting results are illustrated in Table 2. There are some extra diffraction peaks, especially in the

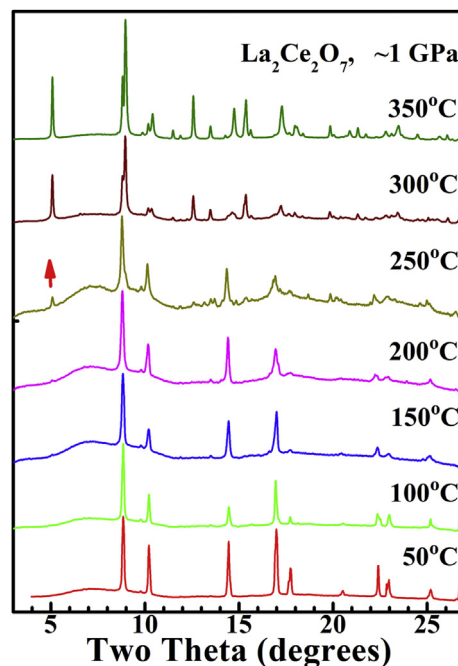


Fig. 6. The XRD profiles of $\text{La}_2\text{Ce}_2\text{O}_7$ measured in a diamond anvil cell at $\sim 1\text{ GPa}$ and temperatures up to 350 °C.

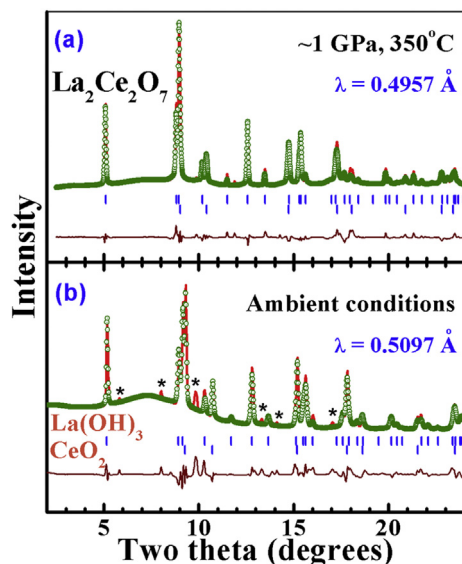


Fig. 7. The Rietveld refinement of the XRD patterns of $\text{La}_2\text{Ce}_2\text{O}_7$ (a) at ~ 1 GPa, 350°C ; (b) quenched from hydrothermal treatment. The majority phase is the hydrate $\text{La}(\text{OH})_3$ and La^{3+} -doped CeO_2 , and some extra diffraction peaks marked with stars are from minor impurity phase(s).

Table 2

The lattice parameters and fitting results of the decomposed phases in $\text{La}_2\text{Ce}_2\text{O}_7$ at 350°C , 1 GPa and quenched from hydrothermal treatment.

	350 °C, 1 GPa	Quenched from 10 GPa, 450 °C
Fitting results	$R_p = 21.8$, $R_{wp} = 17.0$, $\chi^2 = 1.07$ Weight percentage: $\text{La}(\text{OH})_3$: 73.7%, CeO_2 : 26.3%	$R_p = 26.9$, $R_{wp} = 25.6$, $\chi^2 = 2.95$ Weight percentage: $\text{La}(\text{OH})_3$: 68.1%, CeO_2 : 31.9%
$\text{La}(\text{OH})_3$ $P6_3/m$	$a = b = 6.4519$ (5) Å $c = 3.8568$ (3) Å	$a = b = 6.5388$ (10) Å $c = 3.8671$ (9) Å
La: $2c$ ($1/3, 2/3, 1/4$)	$R_{B1} = 13.2$ $R_{f1} = 15.4$	$R_{B1} = 14.1$ $R_{f1} = 11.7$
CeO_2 $Fm-3m$	$a = b = c = 5.4665$ (3) Å	$a = b = c = 5.4514$ (4) Å
Ce: $4a$ (0, 0, 0)	$R_{B2} = 11.7$	$R_{B2} = 8.9$
O: $8c$ ($1/4, 1/4, 1/4$)	$R_{f2} = 10.0$	$R_{f2} = 4.7$

quenched sample, which cannot be identified. The very weak intensities suggest that they come from some minor phases produced during the hydrothermal treatment. The impurity phase has no effect on the identification of the hexagonal hydrate and the cubic CeO_2 phases which is not our interest, and the fitting results are also acceptable.

From the two-dimensional Debye rings recorded on the CCD detector, the growth of crystallites during heating was clearly observed, which affects the intensity fitting of diffraction peaks. However, this effect on the lattice parameters is very limited because lattice constants depend only on the position of individual diffraction peaks. Fig. 8 shows the refined unit cell parameter of the fluorite-type phase at various temperatures. The unit cell constant increases rapidly after 200°C and reaches to a maximum value of 5.5984 Å at 250°C . If there is not major change in the pressure, the unit cell volume should change linearly with temperature. The non-linear increase of the unit cell constant may be due to the incorporation of water into the fluorite structure. Since pyrochlore or defect fluorite oxides possess intrinsic vacancies in the structure, at proper conditions, water and other small molecule can be inserted into the structure and occupy the vacant sites [46,47]. The XRD patterns at temperature of 250°C and 300°C show distinct changes due to the formation of lanthanum hydroxide. In the meanwhile, a very quick drop of the unit cell constant for the cubic phase was

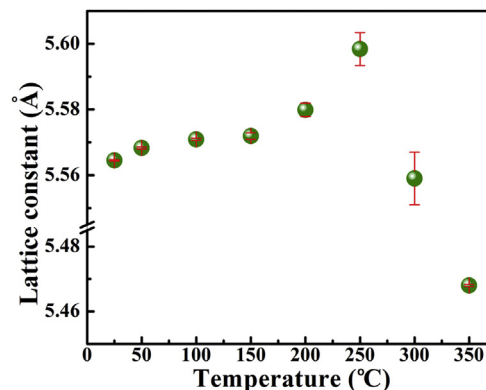


Fig. 8. The lattice parameter of $\text{La}_2\text{Ce}_2\text{O}_7$ cubic phase during hydrothermal process. The cell parameter drops fast after 250°C , which is due to the reaction of La with water, and the cubic phase in the sample is mainly La^{3+} -doped CeO_2 above that temperature.

observed. It decreases from 5.5984 Å at 250°C to 5.468 Å at 350°C . The error bars are derived directly from Rietveld refinement, and large error bars are obtained at temperatures higher than 250°C because of the mixed structures. The fluorite-type cubic phase at

350°C , in fact, is no longer $\text{La}_2\text{Ce}_2\text{O}_7$ because of the reaction between La^{3+} and water. The products should be $\text{La}(\text{OH})_3$ and CeO_2 , though some Ce^{4+} may exist in the hydroxide and La^{3+} in CeO_2 . The cubic phase in the quenched sample has a unit cell parameter of $a = 5.4449$ (4) Å, which is a little larger than that of pure ceria (5.411 Å), but much smaller than that of $\text{La}_2\text{Ce}_2\text{O}_7$ fluorite (5.5642 Å). We propose that the cubic phase after reaction with water is La^{3+} -doped CeO_2 . The refined hexagonal phase has unit cell parameters ($a = b = 6.539$ (1) Å, $c = 3.8671$ (9) Å) very close to those of $\text{La}(\text{OH})_3$ reported in Ref. [48] (6.532 Å, 3.855 Å), which suggests that the hexagonal phase is nearly a pure $\text{La}(\text{OH})_3$. These experimental results indicate that $\text{La}_2\text{Ce}_2\text{O}_7$ is not stable in a moist environment, and the electronic properties of a $\text{La}_2\text{Ce}_2\text{O}_7$ -containing electrode in a solid-oxide fuel cell may deteriorate over time.

4. Summary

The structure of $\text{La}_2\text{Ce}_2\text{O}_7$ with fluorite-type structure was studied by synchrotron XRD at room temperature/high pressure conditions. The fluorite structure is not stable at pressures above 22.6 GPa. The pressure-induced phase transition in $\text{La}_2\text{Ce}_2\text{O}_7$ is reversible when pressure is released. $\text{La}_2\text{Ce}_2\text{O}_7$ fluorite is also not stable under hydrothermal conditions at pressure of ~ 1 GPa and

350 °C and reacts with water to form a hexagonal La-hydroxide and La-doped ceria.

Acknowledgments

This work is supported by Department of Energy (DOE) Stewardship Science Academic Alliances program, National Nuclear Security Administration of the U.S. Department of Energy under award number DE-NA0001977. The XRD measurement was performed at beam 16-BMD, HPCAT, Advanced Photon Source, Argonne National Laboratory. HPCAT operations are supported by DOE-NNSA under Award No. DE-NA0001974 and DOE-BES under Award No. DE-FG02-99ER45775, with partial instrumentation funding by NSF. The Advanced Photon Source is a U.S. Department of Energy (DOE) Office of Science User Facility operated for the DOE Office of Science by Argonne National Laboratory under Contract No. DE-AC02-06CH11357.

References

- [1] K.E. Sickafus, R.W. Grimes, J.A. Valdez, M. Tang, M. Ishimaru, S.M. Corish, C.R. Stanek, B.P. Uberuaga, *Nat. Mater.* 6 (2007) 217.
- [2] A. Meldrum, C.W. White, V. Keppens, L.A. Boatner, R.C. Ewing, *Phys. Rev. B* 63 (2001) 104109.
- [3] K.E. Sickafus, L. Minervini, R.W. Grimes, J.A. Valdez, M. Ishimaru, F. Li, K.J. McClellan, T. Hartmann, *Science* 289 (2000) 748.
- [4] R.C. Ewing, W.J. Weber, J. Lian, *J. Appl. Phys.* 95 (2004) 5949.
- [5] A. Chartier, G. Catillon, J.P. Crocombette, *Phys. Rev. Lett.* 102 (2009) 155503.
- [6] B.J. Wuensch, K.W. Eberman, *JOM-J. Miner. Metals Mater.* 52 (2000) 19.
- [7] J. Lian, L. Wang, J. Chen, K. Sun, R.C. Ewing, J.M. Farmer, L.A. Boatner, *Acta Mater.* 51 (2003) 1493.
- [8] N.J. Hess, B.D. Begg, S.D. Conradson, D.E. McCready, P.L. Gassman, W.J. Weber, *J. Phys. Chem. B* 106 (2002) 4663.
- [9] M.A. Subramanian, G. Aravamudan, G.V. Subba Rao, *Prog. Solid State Chem.* 15 (1983) 55.
- [10] W. Sun, S. Fang, L. Yan, W. Liu, *Fuel Cells* 12 (2012) 457–463.
- [11] P.K. Moon, H.L. Tuller, *Solid State Ion.* 47 (1988) 28.
- [12] S.A. Kramer, H.L. Tuller, *Solid State Ion.* 82 (1995) 15.
- [13] T. Moriga, A. Yoshiasa, F. Kanamaru, K. Koto, M. Yoshimura, S. Somiya, *Solid State Ion.* 31 (1989) 319.
- [14] H. Yamamura, H. Nishino, K. Kakimura, K. Nomura, *Solid State Ion.* 158 (2003) 359.
- [15] E. Reynolds, P.E.R. Blanchard, Q.D. Zhou, B.J. Kennedy, Z.M. Zhang, L.Y. Jang, *Phys. Rev. B* 85 (2012) 132101.
- [16] R. Vaben, F. Traeger, D. Stover, *Int. J. Appl. Ceram. Technol.* 1 (2004) 351.
- [17] S.X. Wang, B.D. Begg, L.M. Wang, R.C. Ewing, W.J. Weber, K.V.G. Kutty, *J. Mater. Res.* 14 (1999) 4470.
- [18] W.J. Weber, R.C. Ewing, *Science* 5487 (2000) 2051.
- [19] P. Nachimuthu, S. Thevuthasan, V. Shutthnandan, E.M. Adams, W.J. Weber, B.D. Begg, D.K. Shuh, D.W. Lindle, E.M. Gullikson, R.C.C. Perera, *J. Appl. Phys.* 97 (2005) 033518.
- [20] J. Lian, X.T. Zu, K.V.G. Kutty, J. Chen, L.M. Wang, R.C. Ewing, *Phys. Rev. B* 66 (2002) 054108.
- [21] J. Lian, L.M. Wang, R.G. Harie, K.B. Helean, R.C. Ewing, *Nucl. Instrum. Methods Phys. Res. B* 218 (2004) 236.
- [22] M. Lang, M. Toulemonde, J.M. Zhang, F.X. Zhang, C.L. Tracy, J. Lian, Z.W. Wang, W.J. Weber, D. Severin, M. Bender, C. Trautmann, R.C. Ewing, *Nucl. Instrum. Methods Phys. Res. B* 336 (2014) 102.
- [23] M. Lang, F.X. Zhang, J.M. Zhang, J.W. Wang, J. Lian, W. Weber, B. Schuster, C. Trautmann, R. Neumann, R.C. Ewing, *Nucl. Instrum. Methods Phys. Res. B* 268 (2010) 2951.
- [24] F.X. Zhang, J. Lian, U. Becker, L.M. Wang, R. Ewing, A.L. Boatner, S. Saxena, J.Z. Hu, *J. Solid State Chem.* 180 (2007) 576.
- [25] D.E.P. Vanpoucke, P. Bultinck, S. Cottenier, V. Van Speybroeck, I. Van Driesche, *Phys. Rev. B* 84 (2011) 054110.
- [26] F. Brisse, O. Knop, *Can. J. Chem.* 45 (1967) 609–614.
- [27] J.S. Bae, W.K. Choo, C.H. Lee, *J. Eur. Ceram. Soc.* 24 (2004) 1291.
- [28] F.X. Zhang, B. Manoun, S.K. Saxena, C.S. Zha, *Appl. Phys. Lett.* 86 (2005) 181906.
- [29] F.X. Zhang, J.W. Wang, J. Lian, M.K. Lang, U. Becker, R.C. Ewing, *Phys. Rev. Lett.* 100 (2008) 045503.
- [30] F.X. Zhang, M. Lang, U. Becker, R.C. Ewing, J. Lian, *Appl. Phys. Lett.* 92 (2008) 011909.
- [31] M. Lang, F.X. Zhang, R.C. Ewing, J. Lian, C. Trautmann, Z.W. Wang, *J. Mater. Res.* 24 (2009) 1322.
- [32] J.M. Zhang, J. Lian, A.F. Fuentes, F.X. Zhang, M. Lang, F.Y. Lu, R.C. Ewing, *Appl. Phys. Lett.* 94 (2009) 243110.
- [33] M. Lang, F.X. Zhang, J. Zhang, J. Wang, B. Schuster, C. Trautmann, R. Neumann, U. Becker, R.C. Ewing, *Nat. Mater.* 8 (2009) 793.
- [34] H.N.H. Yamamura, H. Nishino, K. Kakinuma, K. Nomura, *J. Ceram. Soc. Jpn.* 1300 (2003) 902.
- [35] B. Lin, S.L. Wang, X.Q. Liu, G.Y. meng, *J. Alloy. Compd.* 478 (2009) 355.
- [36] Q.P. Zhang, X. Zheng, J. Jiang, W. Liu, *J. Phys. Chem. C* 117 (2013) 20378.
- [37] L. Yan, W. Sun, L. Ni, S. Fang, Z. Tao, W. Liu, *Int. J. Hydrogen Energy* 35 (2010) 4508.
- [38] A. Hammersley, *Computer Program Fit 2d*, ESRF, Grenoble, 1998.
- [39] Y. Fei, J. Li, K. Hirose, W. Minarik, J. van Orman, C. Sanloup, W. van Westrenen, T. Komabayashi, K. Funakoshi, *Phys. Earth Planet. Inter.* 143–144 (2004) 515.
- [40] T. Roisnel, J. Rodriguez-Carvajal, *Materials science forum*, in: *Proc. 7th Eur. Powder Diffraction Conf. (EPDIC7)*, 118, 2000.
- [41] J.M. Leger, J. Haines, A. Atouf, *J. Phys. Chem. Solids* 57 (1996) 7–16.
- [42] F.X. Zhang, J. Lian, U. Becker, R.C. Ewing, J.Z. Hu, S. Saxena, *Phys. Rev. B* 76 (2007) 214104.
- [43] J.R. McBride, K.C. Hass, B.D. Poindexter, W.H. Weber, *J. Appl. Phys.* 76 (1994) 2435.
- [44] W.H. Weber, K.C. Hass, J.R. McBride, *Phys. Rev. B* 48 (1993) 178.
- [45] W.A. Bassett, *Eur. J. Mineral.* 15 (2003) 773.
- [46] F.X. Zhang, M. Lang, Z.X. Liu, R.C. Ewing, *Phys. Rev. Lett.* 105 (2010) 015503.
- [47] P.W. Bames, P.M. Woodward, Y. Lee, T. Vogt, J.A. Hriljac, *J. Am. Chem. Soc.* 125 (2003) 4572.
- [48] I. Djerdj, G. Garnweitner, D.S. Su, M. Niederberger, *J. Solid State Chem.* 180 (2007) 2154.